PIP_2 controls voltage-sensor movement and pore opening of Kv channels through the S4–S5 linker

Aldo A. Rodriguez-Menchaca[1], Scott K. Adney, Qiong-Yao Tang, Xuan-Yu Meng, Avia Rosenhouse-Dantsker[2], Meng Cui, and Diomedes E. Logothetis[3]

Department of Physiology and Biophysics, Virginia Commonwealth University School of Medicine, Richmond, VA 23298

Edited by Richard W. Aldrich, University of Texas at Austin, Austin, TX, and approved July 20, 2012 (received for review May 11, 2012)

Voltage-gated K^+ (Kv) channels couple the movement of a voltage sensor to the channel gate(s) via a helical intracellular region, the S4–S5 linker. A number of studies link voltage sensitivity to interactions of S4 charges with membrane phospholipids in the outer leaflet of the bilayer. Although the phospholipid phosphatidylinositol-4,5-bisphosphate (PIP_2) in the inner membrane leaflet has emerged as a universal activator of ion channels, no such role has been established for mammalian Kv channels. Here we show that PIP_2 depletion induced two kinetically distinct effects on Kv channels: an increase in voltage sensitivity and a concomitant decrease in current amplitude. These effects are reversible, exhibiting distinct molecular determinants and sensitivities to PIP_2. Gating current measurements revealed that PIP_2 constrains the movement of the sensor through interactions with the S4–S5 linker. Thus, PIP_2 controls both the movement of the voltage sensor and the stability of the open pore through interactions with the linker that connects them.

voltage-gated channels | lipids | channel modulation | open probability

Voltage-gated K^+ (Kv) channels are tetrameric integral membrane proteins critical to membrane excitability that respond rapidly to changes in membrane potential to control membrane permeability to potassium ions. Upon membrane depolarization, a voltage sensor in each subunit undergoes a transition from a resting to an activated state followed by a concerted transition leading to the opening of the pore (1–4). The voltage-sensing domain [i.e., the S1–S4 transmembrane (TM) helices] of Kv channel subunits harbors within its S4 helix several positively charged residues that respond directly to changes in membrane voltage (5–7). The movement of these charges can be monitored by the gating current they produce, and the opening of the pore is monitored by the ionic current that follows. The S4–S5 linker couples the movement of the voltage sensor to the opening of the pore.

X-ray structures of Kv channels have shown that the S1–S4 voltage-sensing domains are exposed to lipids when embedded in a membrane (8, 9). A number of studies have suggested that, after depolarization, interactions of the S4 charges with lipids in the outer leaflet of the membrane are important in the stabilization of the sensor in the activated state (10–12).

Phosphatidylinositol-4,5-bisphosphate (PIP_2), a phospholipid that affects the activity of many types of ion channels (13, 14), acts as a docking platform for the N-terminal domain of fast-inactivating Kv channels (15). Activation of *Ciona intestinalis* voltage-sensitive phosphatase (Ci-VSP), which contains a voltage-sensing domain (S1–S4) coupled to a cytoplasmic phosphatase domain rather than a TM pore, shows a dependence on membrane depolarization similar to that of voltage-gated channels (16). PIP_2 modulates the motions of the Ci-VSP voltage-sensor domain and its coupling to the phosphatase domain by interacting with the linker that connects the voltage sensor and phosphatase domains (17).

In the present study we set out to determine whether PIP_2 modulates the gating mechanism of Kv1.2 channels and to identify specific regions where the lipid might interact to exert its effects. We used a number of different approaches to study PIP_2 depletion effects on the activity of Kv1.2 channel expressed in *Xenopus* oocytes, using the excised patch mode of the patch-clamp technique (18) or the two-electrode voltage-clamp technique on intact oocytes (7).

Results

Dual Effect of PIP_2 on Kv1 Channels. The effects of PIP_2 depletion on Kv1.2 channels expressed in *Xenopus* oocytes were investigated first in excised inside-out macropatches.

Rundown. Following patch excision, into a symmetrical high-K^+ solution (ND96K), current mediated by Kv1.2 channels and activated by depolarizing steps to +60 mV successively decreased in amplitude (to 75% of the cell-attached value) (Fig. 1 *A* and *B Upper*), and the tail current deactivation was slowed successively [~3.5-fold increase in the deactivation time constant (τ_{deact})] (Fig. 1 *C* and *D* and Fig. S1). Similarly, the steady-state activation curve of Kv1.2 was shifted largely to the left following formation of inside–out patches (Fig. 1*G*). The midpoint voltage of activation ($V_{1/2}$) was approximately −67 mV when recorded immediately after patch excision; however, within 10 min of formation of the inside–out patch, the $V_{1/2}$ had shifted by −19 mV, to approximately −86 mV. The time course of rundown for this experiment (τ = 10.7 min) (Fig. S1*A*) was different from the time course of the tail current deactivation and the $V_{1/2}$ shift (τ = 2.3 min and 2.9 min, respectively) (Fig. S1*B*), indicating the existence of two kinetically distinct effects, one on the current amplitude and the other on the voltage sensitivity ($V_{1/2}$ shift and tail current deactivation), following inside–out patch rundown.

To limit the known enzymatic degradation of phospholipids in perfused inside–out patches, a phosphatase inhibitor-containing solution (fluoride, vanadate, pyro-phosphate; FVPP) was used (19, 20). Excision in FVPP solution largely slowed the decay of the Kv1.2 current observed under control conditions (Fig. 1 *A* and *B Lower*). However, the slowdown of the tail current deactivation (Fig. 1 *E* and *F*) and the left shift of the steady-state activation curve (Fig. 1*H*) were still present under these conditions. Thus, phosphatase inhibitors largely delayed the current rundown but did not prevent the changes in Kv1.2 channel tail

Author contributions: A.A.R.-M., A.R.-D., and D.E.L. designed research; A.A.R.-M., S.K.A., Q.-Y.T., X.-Y.M., A.R.-D., and M.C. performed research; A.A.R.-M., S.K.A., Q.-Y.T., X.-Y.M., A.R.-D., M.C., and D.E.L. analyzed data; and A.A.R.-M., A.R.-D., and D.E.L. wrote the paper.

The authors declare no conflict of interest.

This article is a PNAS Direct Submission.

[1]Present address: Departamento de Fisiología y Biofísica, Facultad de Medicina, Universidad Autónoma de San Luis Potosí, San Luis Potosi, SLP 78210, Mexico.

[2]Present address: Pulmonary Section, Department of Medicine, University of Illinois at Chicago, Chicago, IL 60612.

[3]To whom correspondence should be addressed. E-mail: delogothetis@vcu.edu.

See Author Summary on page 14299 (volume 109, number 36).

This article contains supporting information online at www.pnas.org/lookup/suppl/doi:10.1073/pnas.1207901109/-/DCSupplemental.

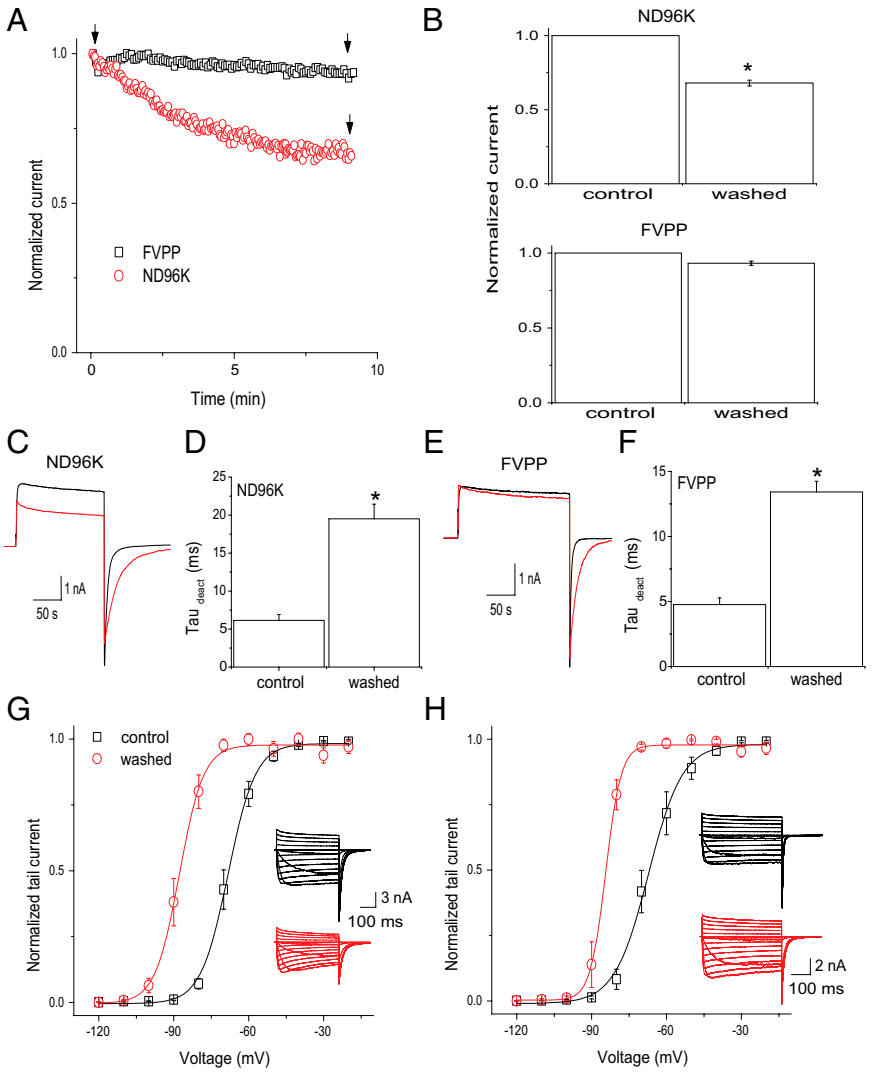

Fig. 1. Effects of ND96K or FVPP perfusion of excised inside–out patches expressing Kv1.2 channels. (*A*) Temporal course of the current amplitude at +60 mV in ND96K (black squares) or FVPP (red circles) solutions. Current is normalized to that obtained immediately after patch excision (labeled as "control" in *B*). (*B*) Average current amplitude after a 10-min perfusion relative to control in ND96K (*Upper*) and FVPP (*Lower*) solutions (± SEM, $n = 5$). (*C*) Representative traces recorded at the time points indicated by the arrows in *A* for ND96K solution. (*D*) Summary of the time constants of tail current deactivation ($_{deact}$) from currents similar to those shown in *C* in control (black) and ND96K-perfused(red) patches for 10 min (± SEM, $n = 5$). (*E*) Representative traces recorded at the time points indicated by the arrows in *A* for FVPP solution. (*F*) Summary of the time constants of tail current deactivation from currents similar to those shown in *E* in control (black) and FVPP-perfused (red) patches for 10 min (± SEM, $n = 5$). (*G*) Steady-state activation curves of Kv1.2 channels determined in control patches (black) and after patches were perfused with ND96K solution for 10 min (red). (*H*) Steady-state activation curves of Kv1.2 channels determined in control patches (black) and after patches were perfused with FVPP solution for 10 min (red). Data points in *G* and *H* are mean ± SEM ($n = 5$). Lines are fits of a Boltzmann function to the data. *$P < 0.05$ versus control.

current deactivation and $V_{1/2}$, suggesting differential PIP_2 sensitivities of these two PIP_2-dependent effects.

PIP_2 antibody. We then examined the effect of reducing endogenous PIP_2 levels by applying an antibody specifically recognizing PIP_2 (PIP_2-Ab) directly to inside–out patches (19). Application of PIP_2-Ab caused a 25% reduction of the current amplitude at +60 mV (Fig. 2 *A–C*), an effect similar to the rundown results shown above (i.e., Fig. 1 *A* and *B Upper*). In addition to the blocking of current amplitude, effects on the tail current deactivation kinetics and $V_{1/2}$ (similar to the rundown results shown in Fig. 1) were observed. PIP_2-Ab caused a slowdown of the tail current deactivation kinetics (Fig. 2 *D* and *F*) and an ∼14-mV leftward shift in the voltage dependence of activation (Fig. 2*E*), indicating that the reduction in PIP_2 levels caused a pronounced stabilization of the voltage-dependent activated state of the channel. All three effects were reversed to the control conditions by applying exogenous PIP_2 to the excised patches (Fig. 2). Similar results were obtained with the Shaker K^+ channel (a *Shaker* variant in which the inactivation domain was removed; Shk-IR) (Fig. S2).

Wortmannin. In addition to manipulating PIP_2 levels in inside–out patches, we examined the effects of reducing PIP_2 levels in the plasma membrane of intact oocytes. The activity of Kv1.2 channels expressed in *Xenopus* oocytes was recorded with the two-electrode voltage-clamp technique under control conditions and after the oocytes were preincubated for 2 h with 20 μM wortmannin, an inhibitor of the type-III PI 4-kinase at micromolar concentrations (21). As illustrated in Fig. 3 *A* and *B*, Kv1.2 channels were activated upon depolarizing voltage steps. Wortmannin caused a decrease in the current amplitude, measured in a voltage step where all of the channels were fully activated (Fig. 3*C*). Independently of this effect on the current level, Kv1.2

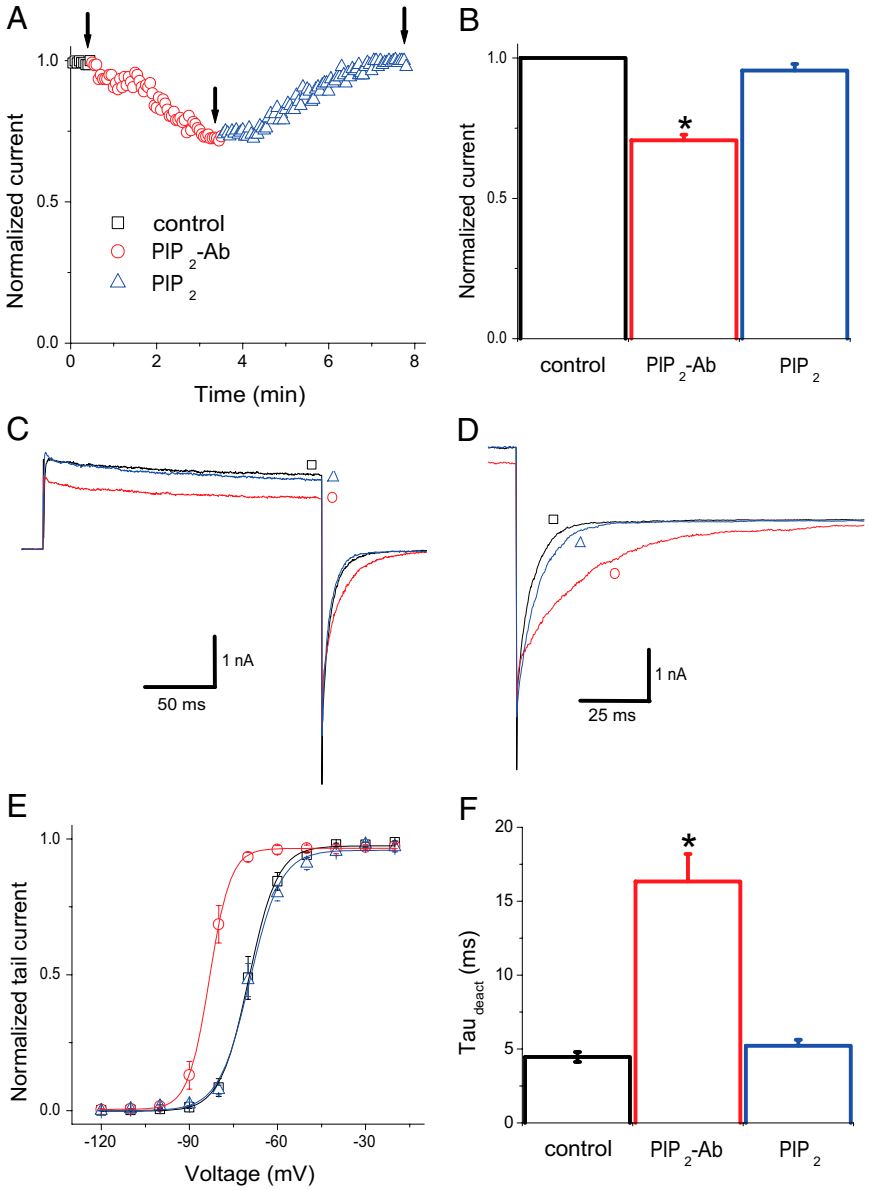

Fig. 2. PIP_2-Ab–mediated effects on voltage-dependent gating and current amplitude of Kv1.2 channels are reversed by PIP_2. (*A*) Temporal course of the Kv1.2 current amplitude at +60 mV before (black) and during (red) PIP_2-Ab application and during PIP_2 (blue) application. (*B*) Summary of the effects of PIP_2-Ab and PIP_2 on current amplitude (± SEM, $n = 5$). (*C*) Representative traces recorded at the time points indicated by the arrows in *A*. (*D*) Deactivation of Kv1.2 tail currents in control channels and with PIP_2-Ab and PIP_2 application. (*E*) Steady-state activation curves of Kv1.2 channels determined before (black) and after application of 10 μg/mL PIP_2-Ab (red) and during subsequent application of 10 μM PIP_2 (blue). Data points are mean ± SEM ($n = 6$). Lines are fits of a Boltzmann function to the data. (*F*) Summary of the time constants of deactivation (τ_{deact}) from tail currents similar to those shown in *D* in control channels and with PIP_2-Ab and PIP_2 application (± SEM, $n = 5$). *$P < 0.05$ versus control.

channels in oocytes pretreated with wortmannin required lower depolarizing voltage steps for equivalent activation than channels recorded under control conditions. Wortmannin treatment led to a left shift of channel activation by >10 mV, with $V_{1/2}$ = −21.64 mV and −31.90 mV as determined with Boltzmann fits to the mean steady-state activation of control and wortmannin-treated Kv1.2 channels, respectively (Fig. 3*D*). In addition, wortmannin caused a decrease in the rate of the tail current deactivation (Fig. 3*E*).

Ci-VSP. We also depleted PIP_2 in intact oocytes with Ci-VSP (16). Reversible PIP_2 depletion can be achieved after membrane depolarization to activate Ci-VSP. Ci-VSP was coexpressed with the channel, and its activity was controlled with the voltage protocol shown in Fig. 4*A*, *Upper* in the whole-cell configuration, using the two-electrode voltage-clamp technique. An up-ramp protocol from −80 to +60 mV was applied first and was used as a control (resting PIP_2 levels before the voltage protocol reached 0 mV), and a second, down-ramp protocol from +60 to −80 mV was applied after the oocytes were held at +60 mV for 3 s for partial depletion of PIP_2 from the plasma membrane. Application of the up- and down-ramps in oocytes expressing Kv1.2 channels alone produced nearly indistinguishable linear currents (Fig. 4*A*, *Lower*); the difference in the voltage at 10% of activation ($\Delta V_{1/10}$) between the up- and down-ramps was 2.28 ± 0.43 mV ($n = 4$). Activation of Ci-VSP during the up-ramp (>0 mV) caused a decrease in current amplitude, as can be seen by the deviation of current from linearity, whereas application of the down-ramp in addition to a further decrease in current ampli-

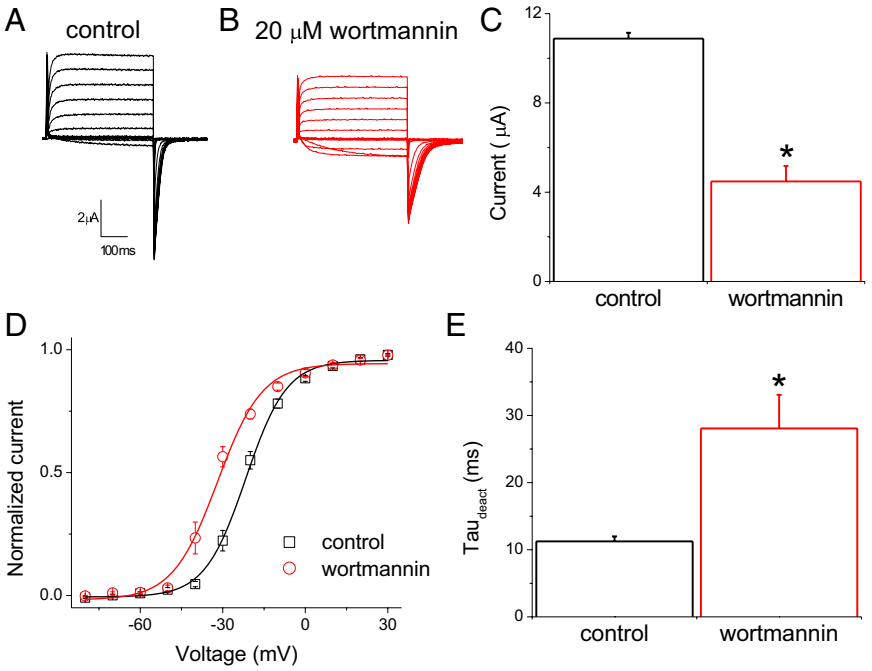

Fig. 3. Modulation of Kv1.2 channel currents by wortmannin. (*A* and *B*) Representative whole-cell current traces from oocytes expressing Kv1.2 channels evoked by depolarizing voltages from −80 to +60 mV followed by a step to −80 mV for tail current analysis preincubated for 120 min in control (*A*) or wortmannin (*B*) solutions. (*C*) Average amplitude of Kv1.2 channels at +60 mV (± SEM, $n = 5$). (*D*) Steady-state activation curves of Kv1.2 channels determined in control (black) and wortmannin-treated (red) oocytes. Data points are mean ± SEM ($n = 5$). Lines are fits of a Boltzmann function to the data. (*E*) Summary of time constants of tail current deactivation (τ_{deact}) in control and wortmannin-treated oocytes (± SEM, $n = 5$). *$P < 0.05$ versus control.

tude also showed a shift in the voltage dependence of activation (Fig. 4*B*), with a $\Delta V_{1/10}$ of 13.44 ± 1 mV ($n = 6$). Finally, coexpression of Kv1.2 with the catalytically inactive Ci-VSP mutant (C363S) showed currents similar to those in oocytes expressing Kv1.2 alone (Fig. 4*C*), with a $\Delta V_{1/10}$ of 2.34 ± 0.3 mV ($n = 6$). These results in whole-cell recordings recapitulated and confirmed the results in excised patches with regard to the PIP_2-mediated effects on the current amplitude and voltage sensitivity of Kv1.2 channels. Just as with excised patches, the two effects on current amplitude and voltage dependence of activation mediated by Ci-VSP were kinetically distinct: Although the recovery of the shift in the voltage dependence of activation took only several milliseconds (Fig. S3 *A* and *B*), the recovery of current amplitude required >25 s of repolarization before reaching control levels (Fig. S3 *C* and *D*). Taken together, these results in both excised patches and intact oocytes suggest that PIP_2 modulates the current amplitude and voltage dependence of activation of Kv channels by distinct mechanisms (Figs. 1–4 and Figs. S1–S3).

Voltage Dependence and Channel Gating Possess Distinct Sensitivities to PIP_2. The rundown experiments in ND96K and FVPP solutions (Fig. 1) suggested differential sensitivities of the two PIP_2-dependent effects on the phosphoinositide. The soluble dioctanoylglycerol-PIP_2 (diC8-PIP_2) is commonly used to quantify the sensitivity of a channel to PIP_2; unlike long-chain PIP_2 analogs, the effects of diC8-PIP_2 are readily reversible, making it possible to construct dose–response curves. We examined the diC8-PIP_2 sensitivity of the two related effects that we observed in Kv1.2 channels. The application of increasing concentrations of diC8-PIP_2 to inside–out patches speeds up the tail current deactivation kinetics (Fig. 5) and shifts back the voltage-dependent activation to depolarized potentials with an estimated EC_{50} of 71.4 ± 15.2 μM (Fig. 5*B*; the maximum $\Delta V_{1/2}$ was set to 14 mV, the value obtained in our PIP_2-Ab experiments). Interestingly, application of diC8-PIP_2 did not recover the current amplitude of the channel even at concentrations as high as 300 μM, suggesting that the current amplitude and voltage dependence of activation possess distinct sensitivities to PIP_2. Fig. 5 *C* and *D* shows temporal courses of the current amplitude measured at +60 mV (Fig. 5*C*) and of the rate of tail current deactivation (Fig. 5*D*) after application of 10 μg/mL PIP_2-Ab, 30 μM diC8-PIP_2, and 10 μM long-chain PIP_2. The application of PIP_2-Ab decreased the Kv1.2 current amplitude and the rate of tail current deactivation, as was seen in our previous experiments; however, application of 30 μM diC8-PIP_2 did not have any effect on current amplitude but partially recovered the rate of tail current deactivation. Subsequent application of long-chain PIP_2 recovered both the current amplitude and rate of tail current deactivation to levels comparable with those before the application of PIP_2-Ab (Fig. 5 *C* and *D*).

PIP_2 Increases Activity by Affecting the Open Probability of Kv1.2 Channels. PIP_2 rundown or depletion by chelating agents (e.g., PIP_2-Ab) decreased the macroscopic conductance, whereas PIP_2 perfusion had the opposite effect. We turned to single-channel recording to examine whether the effects of PIP_2 involved the channel open probability, unitary conductance, or the number of active channels in the patch ($I = NP_oi$, where I is the macroscopic current, N the number of active channels, Po the open probability, and i the unitary current). Fig. 6*A* shows representative activity from a single channel in an inside–out patch held at either −60 mV or +60 mV under rundown conditions or following application of PIP_2. At both voltages PIP_2 increased the open probability without changing the unitary current size. A comparison of the unitary conductance from patches under rundown conditions vs. conditions of PIP_2 application showed similar values at ∼15 pS (Fig. 6*B*). In contrast, PIP_2 yielded a fourfold increase in open probability from patches containing a single channel (Fig. 6*C*). Patches that contained multiple channels yielded an ∼fourfold stimulation in *NPo* similar to that seen in single-channel patches, suggesting that the open proba-

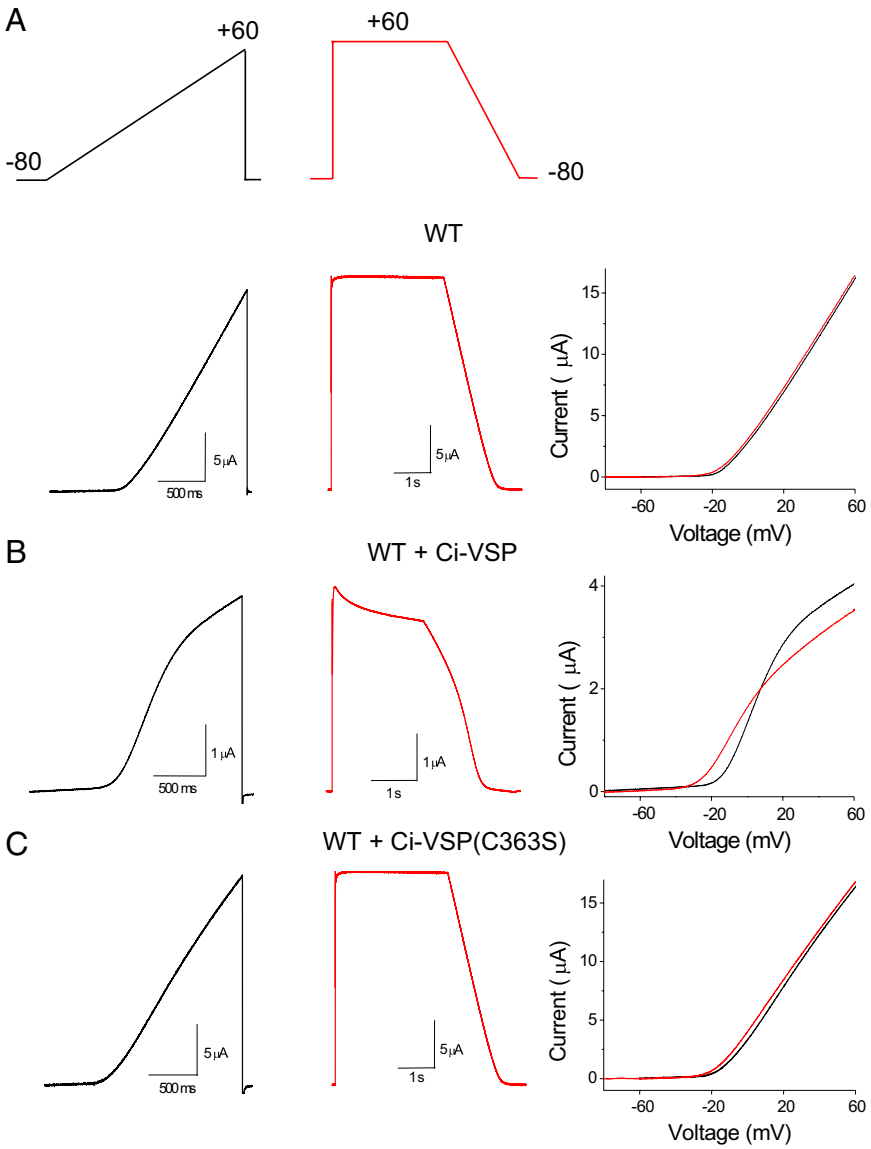

Fig. 4. Modulation of Kv1.2 channel voltage-dependent gating and current amplitude by Ci-VSP. (*A*) Representative current traces evoked by the ramp pulses (*Upper*) for oocytes expressing Kv1.2 channels alone (*Lower*), coexpressed with Ci- VSP (*B*), and with the catalytically inactive mutant C363S of Ci-VSP (*C*). Rightmost panels in *A, B,* and *C* show the current–voltage relationships (up-ramp is black and down-ramp is red) from the representative traces.

bility, rather than the number of active Kv1.2 channels, was affected by PIP_2.

Molecular Determinants for Dual Effects of PIP_2 on Kv1 Channels. We next asked whether the two distinct PIP_2-dependent effects on Kv channels we have described are controlled by different molecular determinants. We hypothesized that, as with other proteins, positively charged amino acids could be involved in electrostatic interactions with PIP_2 in the plasma membrane and that these interactions might be responsible for the PIP_2 effects observed in Kv1.2 channels (22). To identify molecular determinants involved in PIP_2 regulation, we mutated a number of positively charged residues in the N and C termini and in the S4–S5 linker of the Kv1.2 channel. Fig. 7 *A* and *B* shows that K322Q (in the S4–S5 linker) and R147Q (in the N terminus) caused a larger shift in the voltage dependence of activation, as compared with wild-type channels, when PIP_2-Ab was applied to inside–out patches. Similar results were obtained in whole-cell recordings coexpressing the Kv1.2 channels with Ci-VSP (Fig. S4). Fig. 7 *C* and *D* shows that K322Q, but not R147Q, also exhibited a significant reduction in the current amplitude seen by PIP_2-Ab application compared with the wild type. Moreover, the S4–S5 linker mutant R326Q caused a significant change in the current amplitude but not in the voltage sensitivity. These data indicate that R147Q and R326Q affect only voltage sensitivity and current amplitude, respectively, but K322Q affects both.

Interactions of the S4–S5 Linker with PIP_2 Are Coupled to the Voltage Sensitivity and Gating Machineries of Kv1 Channels. Next we investigated whether the presence of PIP_2 could cause changes in the Kv channel structure. Crystal structures of part of the Kv1.2 channel in the open state have been reported (8, 23). We proceeded to dock PIP_2 to a Kv1.2 homology model of the open conformation based on these structures (*Methods*) as well as to a model of the closed state (24, 25). Localization of the three residues whose mutation altered PIP_2-dependent effects on Kv1 channels suggested that PIP_2 could engage all three residues in the closed (Fig. 8 *A* and *C*) but not in the open (Fig. 8*B*) con-

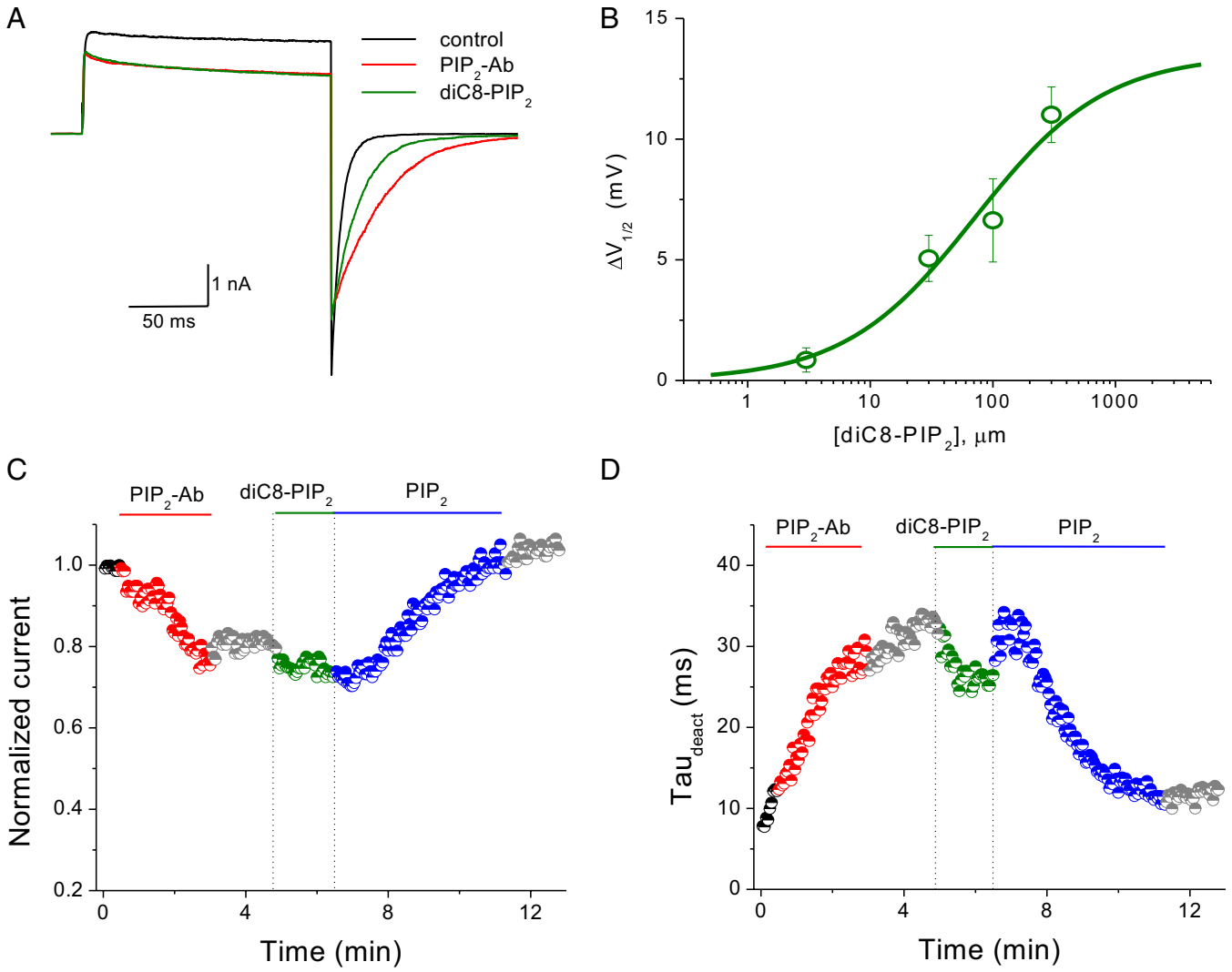

Fig. 5. diC8-PIP_2 restores the voltage-dependent gating of Kv1.2 channels but fails to recover the current amplitude. (*A*) Representative current traces evoked by a pulse to +60 mV from a holding potential of −120 mV before (black) and after (red) application of 10 μM PIP_2-Ab and during subsequent application of 10 μM diC8-PIP_2 (green). (*B*) Dose–response curve for the $\Delta V_{1/2}$ as a function of the concentration of diC8-PIP_2. Data points are mean ± SEM (n = 3–4). Data were fit with the Hill equation. The maximal $\Delta V_{1/2}$ was fixed at 14 mV (the maximum shift recorded) during the adjustment). (*C*) Temporal course of the current amplitude at +60 mV in control (black) channels and with PIP_2-Ab (red), diC8-PIP_2 (green), or long-chain PIP_2 (blue) application. Current is normalized to that obtained immediately after patch excision. (*D*) Temporal course of the time constant of tail current deactivation (τ_{deact}) color-coded as in *C*. Experiments in *C* and *D* were repeated four times.

formation. In the open conformation K322 still could interact with PIP_2, but R147 has moved quite far from the putative PIP_2 binding site, and the rotation of R326 in this conformation would prevent it from interacting with PIP_2 (Fig. 8*B*). The crystal structure of the Kv1.2/Kv2.1 chimera depicts a lipid bound to the S4–S5 region, but this lipid does not interact with any of the three residues we identified (8). Interestingly, in the model of the closed conformation of Kv1.2 (24, 25), the three key residues (R147, K322, and R326) are oriented so that they all can interact with PIP_2 simultaneously (Fig. 8 *A* and *C*), similar to the manner in which PIP_2 interacts with Kir2.2 in the crystallographic structure (*Discussion*) (26). We next performed molecular dynamics (MD) simulations of our open-state homology model in the absence (Apo) and presence (Holo) of PIP_2 and a combined principal components analysis (PCA), using a trajectory from the MD simulations that concatenated the equilibrated trajectories (50–100 ns) in the Apo and Holo conditions. Fig. 8*D* displays the first eigenvector of the combined PCA for one subunit in the absence (red) and presence (blue) of PIP_2 to depict the collective motions of Kv1.2 caused by PIP_2. Significant PIP_2-induced movements were seen in several segments of the channel implicated in the gating mechanism of Kv1 channels.

The presence of PIP_2 caused significant movements; furthermore, these movements were correlated. The largest changes observed in the correlated movement of K322 in the S4–S5 linker were with residues in the selectivity filter (SF) and the S2 and S3 regions following PIP_2 binding (Fig. S5 *A* and *C*). Quantification of these changes revealed increased correlation in the movements of the S4 helix (at K322) with the S2 and S3 residues but a decrease in the correlation with the SF. Fig. S5*D* highlights these residues in the open conformation of the channel.

Disruption of Critical S4–S5 Linker Interactions with PIP_2 Removes a Restraint in Voltage-Sensor Movement. Could PIP_2 directly affect the voltage-sensor movement, thereby controlling the voltage sensitivity of the channel? To address this question, we examined the effect of reducing endogenous PIP_2 levels or channel–PIP_2 interactions on gating currents. For these experi-

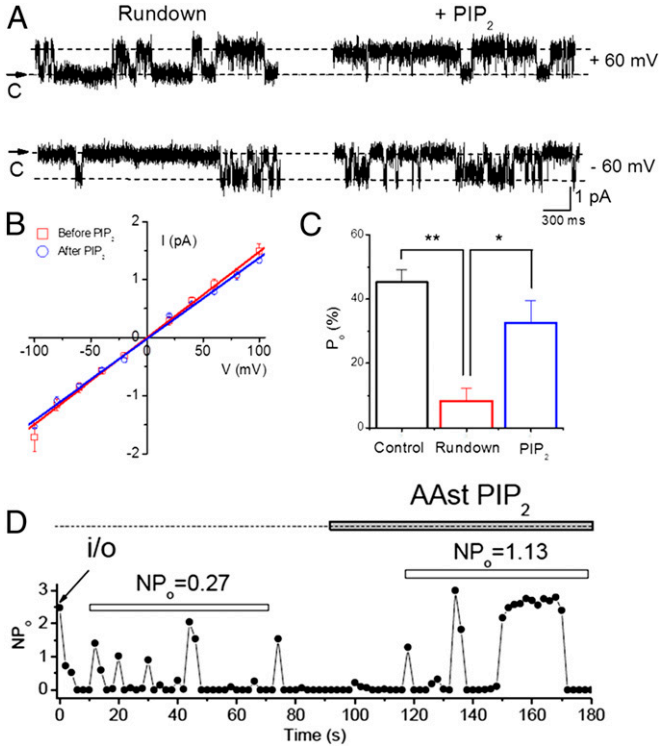

Fig. 6. PIP_2 increases open probability but not the unitary conductance or number of active channels. (*A*) Comparison of Kv1.2 single-channel current traces before (at the end of the rundown period) (*Left*) and after application of PIP_2 (*Right*), held at a membrane potential of either −60 (*Lower*) or +60 mV (*Upper*). Single-channel current traces of Kv1.2 were recorded from excised inside–out patches. Arrows indicate the zero current level (closed state of channels). (*B*) Comparison of Kv1.2 i–V relationships between unitary conductances in the absence (γ = 15.5 pS, n = 5) (red) and presence (γ = 14.2 pS, n = 6) of PIP_2 (blue). i–V relationships were measured with symmetrical 96 mM K-MeS. (*C*) Summary of the single-channel open probability (Po) for Control (following patch excision; NPo = 45.2 ± 4%), rundown (just before PIP_2 application; NPo = 8.4 ± 4%), and after application of 10 μM PIP_2 in the bath (NPo = 32.6 ± 7%). (*D*) Activity (NPo) versus time plot of a representative inside–out patch containing multiple Kv1.2 channels. The filled horizontal bar indicates the time period of PIP_2 application in the bath. The open horizontal bars indicate the same length of time used to calculate NPo from the first appearance of activity in the rundown or the PIP_2 conditions. $^{**}P < 0.01$, $^{*}P < 0.05$.

ments, we used the well-studied ShK-IR channel for ionic current meaurements and its nonconducting W434F mutant (ShK-W434F) for gating current measurements (Fig. 9 *A* and *B*, respectively). Wortmannin treatment induced a leftward shift in the voltage dependence of activation of *Shaker* ionic and gating currents (Fig. 9 *C* and *D*, respectively). Following PIP_2 depletion, just as with Shaker ionic current deactivation under PIP_2-Ab conditions (Fig. S2*D*), the rate of the off-gating currents was slowed under wortmannin conditions (Fig. 9*I*). Prompted by effects of S4–S5 linker mutants on Kv1.2 channels, we mutated two positively charged residues in the *Shaker* S4–S5 linker, creating a chimeric channel with a linker identical to that of Kv1.2 (K322Q). The *Shaker* S4–S5 R387Q-K390Q double mutant caused a leftward shift in the voltage dependence of activation of *Shaker* ionic and gating current (Q_{on}) (Fig. 9 *E* and *F*, respectively) as well as a slow down in the off-gating current (Fig. 9*I*). These PIP_2-mediated effects on ionic and gating currents have been summarized in the ionic current-to-voltage (I–V) and gating current-to-voltage (Q–V) curves shown in Fig. 9 *G* and *H*, respectively. Thus, these experiments suggest that PIP_2 constrains the voltage-sensor movement of Kv channels through interactions with positively charged residues in the S4–S5 linker (i.e., K322) and possibly other participating sites (e.g., R147) of Kv channels that may come together in the 3D closed conformation to contribute to the PIP_2 binding site.

Discussion

In the present work we found that PIP_2 exerts two distinct effects on Kv channels. First, PIP_2 stabilizes the voltage sensor of Kv channels in a state of decreased sensitivity (Q–V and I–V are right shifted), favoring the closed state of the channel. Second, PIP_2 stabilized the Kv channel pore in the conducting state. These two apparently contradictory effects could be separated by differences in kinetics (Figs. S1 and S3), sensitivities to PIP_2 (Figs. 1 and 5), and molecular determinants (e.g., R147 influenced only the PIP_2 effect on voltage sensitivity but not on the macroscopic current; Fig. 7 and Fig. S4).

Most actions of PIP_2 that occur through binding to specific protein sites involve electrostatic interactions between the negatively charged head-group of PIP_2 and positively charged amino acid residues at the target site. This interaction has been demonstrated for direct PIP_2 regulation of several ion channels (27). PIP_2 interacts with Kir channels engaging several intracellular sites, most of which are positively charged residues (20, 28). Similarly, positive residues just after the end of S6 are thought to contribute to the PIP_2 sensitivity of KCNQ1/KCNE1 channels

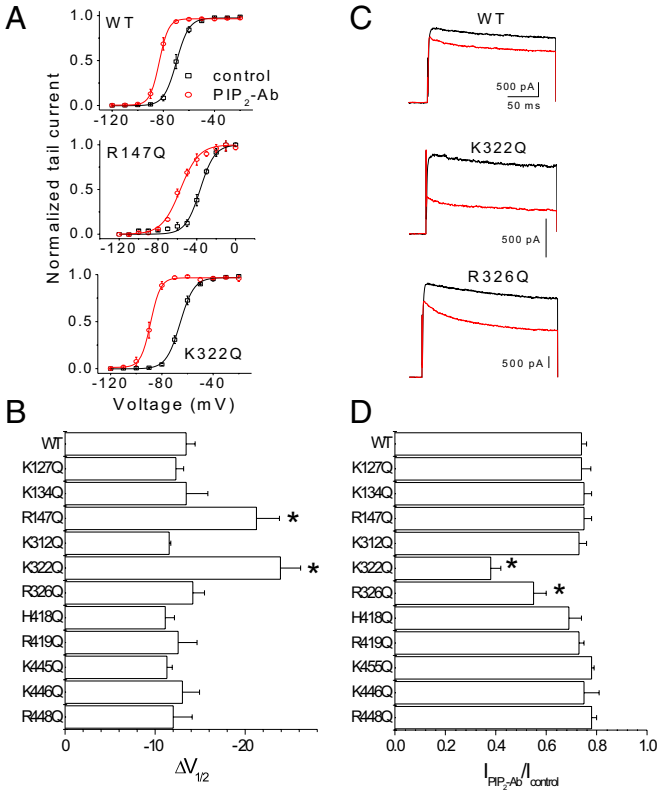

Fig. 7. Distinct determinants of the dual effects of PIP_2 and structural consequences of channel–PIP_2 interactions via the S4–S5 linker. (*A*) Steady-state activation curves of Kv1.2 wild-type and mutant (K322Q and R147Q) channels determined before (black) and after (red) application of 10 μg/mL PIP_2-Ab. Data shown are ± SEM; n = 4–5. (*B*) Average shift in $V_{1/2}$ shown in response to PIP_2-Ab in Kv1.2 wild-type and mutant channels. Data shown are ± SEM; n = 3–5. (*C*) Representative current traces at +60 mV before and after PIP_2-Ab application in Kv1.2 wild-type and mutant (K322Q and R326Q) channels. (*D*) Fraction of current not blocked by PIP_2-Ab (antibody/control) in Kv1.2 wild-type and mutant channels. Data shown are ± SEM; n = 3–5. $^{*}P < 0.05$ versus control.

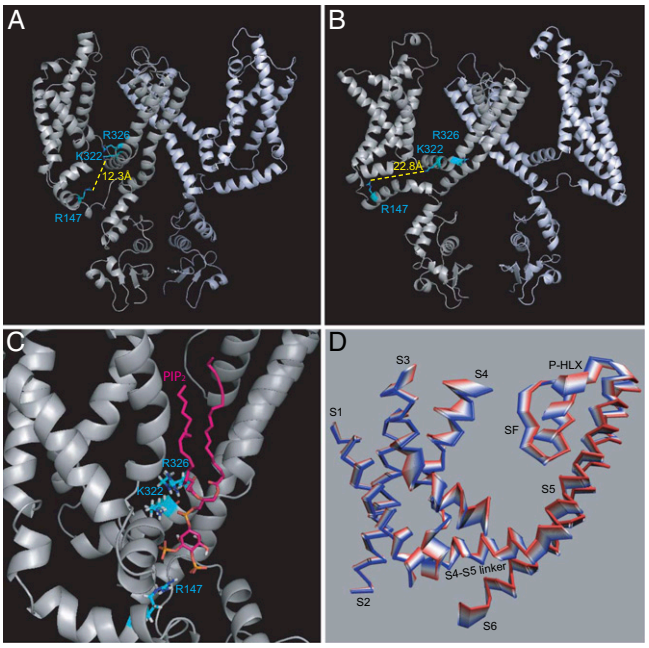

Fig. 8. PIP_2 interactions with critical Kv1.2 residues in the closed conformation affect the motion of critical components of the gating machinery. (*A*) A model of the closed conformation of Kv1.2 (24, 25) showing the distance between the side-chains of R147 and K322. (*B*) A model of the open conformation of the Kv1.2 (*Methods*) showing the distance between the side-chains of R147 and K322. (*C*) A model of the closed structure of Kv1.2 illustrating how PIP_2 could bind to the channel, engaging all three critical residues identified by the experiments shown in Fig. 7. (*D*) PCA analysis showing the collective movements of a Kv1.2 subunit from the absence of PIP_2 (red) to the presence of PIP_2 (blue). Flexible loops were removed from the structures shown to illustrate better the PIP_2-induced collective movements of less flexible regions.

(29). Here our data suggest that the PIP_2-induced effects involve interactions with positively charged residues in the S4–S5 linker (Figs. 7–9), a region responsible for the coupling between the voltage sensor and the pore domain in Kv channels. This interaction directly modulates the movement of the voltage sensor (Fig. 9) and maintains high activity of the channel, possibly by stabilizing the coupling between the sensor and the pore. It has been shown that prolonged depolarizations shift the Q–V relationship of voltage sensor-containing proteins to the left, a process that has been referred to as "relaxation" (30). The effects of PIP_2 depletion or of weakening the interactions of the S4–S5 linker on the Q–V relationship (Fig. 9*H*) were reminiscent of relaxation. Whether prolonged depolarization causes relaxation by decreasing the affinity of the S4–S5 linker to PIP_2 through electrostatic repulsion remains to be examined.

The voltage sensitivity of Kv channels has been shown to be regulated by negatively charged lipids other than PIP_2, including ceramide-1-phosphate (11), and polyunsaturated fatty acids (31). However, this modulation involves channel interactions with the external leaflet of the bilayer, where these lipids are localized. In contrast, the modulation of the channel by PIP_2 is confined to the inner leaflet of the plasma membrane, and its magnitude could be under dynamic control.

Collectively, our data support a model in which positive residues in the N terminus and the S4–S5 linker (e.g., R147, K322, and R326) interact with PIP_2. In the Kir2.2 structure in complex with PIP_2, R78 and R80 are located at the interface between the TM and cytosolic domains of Kir2.2, and their side-chains point in the same direction (26). Similarly, in the proposed model of the PIP_2 binding site in the closed conformation of Kv1.2 (Fig. 8*C*), the 1′ phosphate of PIP2 interacts with K322 and R326, which are located in the S4–S5 linker in proximity to the loop that connects the linker to the S5 TM helix and at the interface between the cytosolic and TM domains. Like the orientation of R78 and R80 in the structure of Kir2.2 in complex with PIP_2, the side-chains of K322 and R326 point in the same direction in the closed conformation of Kv1.2. Furthermore, like the binding site of PIP_2 in Kir2.2, where the acyl chains interact with hydrophobic residues in the TM helices, in the proposed binding site of PIP_2 in Kv1.2 the acyl chains insert into the membrane where they can interact with the hydrophobic amino acids in S3, S5, and possibly S4 (Fig. S5). With the acyl chains and 1′ phosphate of PIP_2 interacting with the TM domain, the inositol ring is oriented toward the cytosolic domain (as in Kir2.2) and interacts with R147.

As the voltage sensor transitions from the resting to the activated state, the S4–S5 residue interactions exert a dual effect. On one hand, they constrain the movement of the voltage-sensing domain; on the other hand, they stabilize the opening of the pore, presumably by constraining the linker with PIP_2 and achieving stronger coupling between the voltage-sensing domain and the pore. K322 was the only residue identified that is predicted to interact with PIP_2 in both the open and closed states. K322 neutralization also was the only residue mutation that affected the stability of both the voltage-sensing domain and the pore. In contrast, R326, which was predicted to interact with PIP_2 only in the closed-state model, did not affect voltage sensitivity, possibly because the upstream interaction between K322 and PIP_2 was still intact. It is possible that mutation of R326 affects the PIP_2-dependent pore stability indirectly by altering the K322–PIP_2 interactions. This suggestion will require validation by further experimental tests. Furthermore, our mutagenesis efforts did not yield insights on molecular determinants of the slow PIP_2 effects on the macroscopic current. Could the stability of the pore also involve cytosolic determinants other than the S4–S5 linker, as is the case in Kir channels? The lack of experimental and structural insights implicating the cytosolic domains of Kv1 channels in interactions with PIP_2 makes it difficult to answer this question at the present time. Clearly, a more complete molecular understanding of how PIP_2 exerts its slow control of the conducting open conformation of the channel will be needed.

The dual effect of PIP_2 on voltage sensitivity and on the stability of the open state also has been shown for voltage-gated N- and P/Q-type Ca^{2+} channels (32). Although currently untested, it is possible that the S4–S5 linker of Ca_v channels, as in Kv channels, is critically involved in mediating the effects of PIP_2. On the other hand, as is the case for Ca_v channels, it is likely that activation of membrane receptors that dynamically deplete PIP_2 levels in excitable cells also has important consequences for cell excitability through modulation of Kv channel activity.

It is likely that recognition of the key role PIP_2 plays in the activation of highly voltage-dependent channels, such as Ca_v and Kv channels, will stimulate the search for a deeper structural understanding of how PIP_2 interacts with full-length Kv channels and how physiological modulation of phosphoinositide levels affects cellular excitability.

Methods

Molecular Biology and Channel Expression in Oocytes. Plasmids rKv1.2-pXoom, Ci-VSP-sp64t, Shaker H4-pBSTA with N-type inactivation removed (Δ6–26) (Shk-IR), and Shaker W434F-pBSTA were used. The cDNA was linearized, and cRNA was prepared using the MessageMachine kit (Ambion). Point mutants were introduced by *Pfu*-based mutagenesis using the QuikChange TM kit (Stratagene). The mutations were verified by sequencing. *Xenopus* oocytes were injected with different concentrations of the RNAs used, depending on the expression level of the given protein.

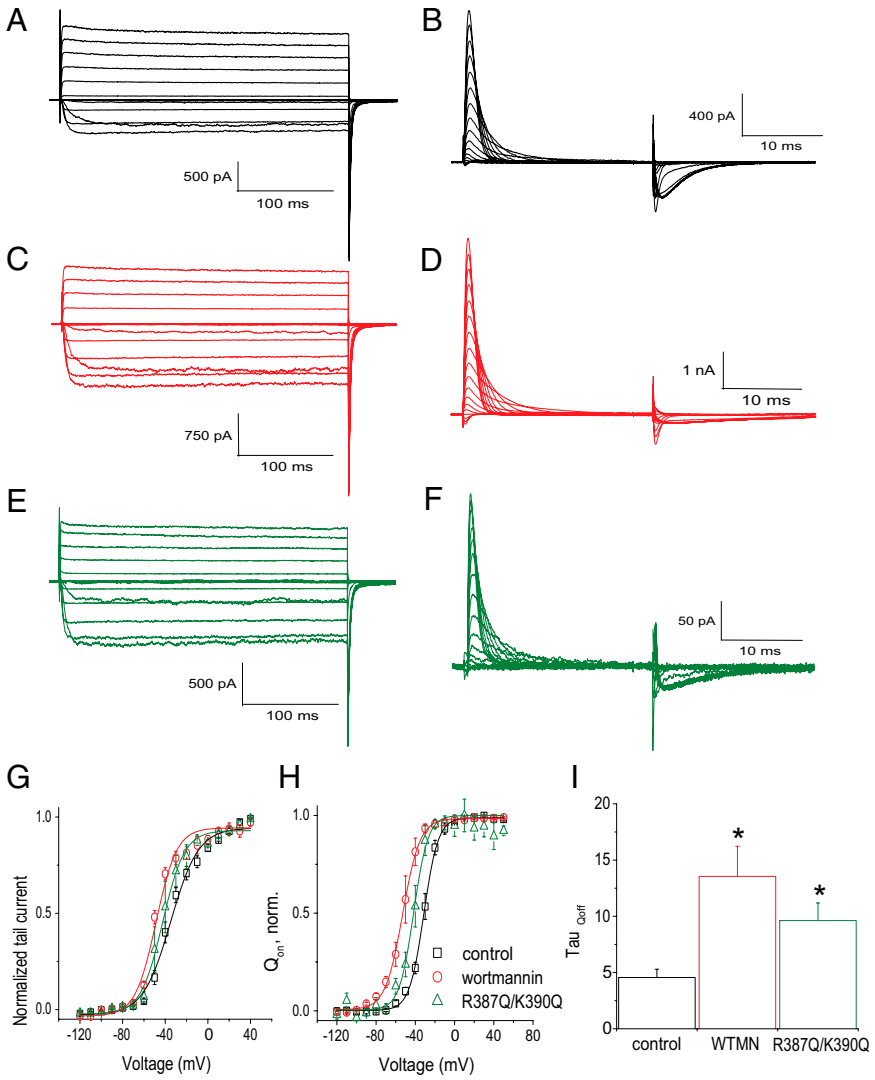

Fig. 9. Effect of PIP_2 depletion on ionic and gating currents of Shk-IR. (*A* and *B*) Representative traces of Shk-IR ionic currents (*A*) evoked by depolarizing voltages from −120 to +50 mV followed by a step to −90 mV for tail current analysis and of ionic current-removed Shaker-W434F (Shk-W434F) gating currents (*B*) evoked by depolarizing voltages from −120 to +50 mV followed by a step to −90 mV. (*C* and *D*) Representative traces of Shk-IR ionic currents (*C*) and Shk-W434F gating currents (*D*) after wortmannin treatment (2 h in 50 μM wortmannin). (*E* and *F*) Representative traces for Shk-IR (R387Q-K390Q) ionic currents (*E*) and for Shk-W434F(R387Q-K390Q) gating currents (*F*). (*G*) Current–voltage relationships for Shk-IR control, wortmannin-treated, and Shk-IR(R387Q-K390Q) channels. Data shown are ± SEM; n = 4–7. (*H*) Charge–voltage relationships for Shk-W434F controls, wortmannin-treated, and Shk-W434F(R387Q-K390Q) channels. Data shown are ± SEM; n = 4–5. (*I*) Summary of the time constants (τ) of the off-gating currents for Shk-W434F (control), wortmannin-treated, and the R387Q-K390Q mutant. Data shown are ± SEM; n = 4–5. *$P < 0.05$ versus control.

Electrophysiology. Recordings in *Xenopus* oocytes were performed 24–72 h after RNA injection. Currents in whole oocytes were measured by conventional two-electrode voltage-clamp with a GeneClamp 500 amplifier (Molecular Devices). Electrodes were filled with 1.5% (wt/vol) agarose in 3 M KCl. The electrodes had resistances of 0.5–1 MΩ. Oocytes were perfused with a high-potassium solution containing (in mM) 96 KCl, 1 NaCl, 1 $MgCl_2$, and 5 Hepes, pH 7.4. A low-potassium solution was used in experiments coexpressing Kv1.2 channels and Ci-VSP, containing (in mM) 96 NaCl, 2 KCl, 1 $MgCl_2$, and 5 Hepes, pH 7.4. Data acquisition and analysis were carried out using pClamp8 (Molecular Devices) and Origin 7 (Microcal) software.

Macropatch channel activity was recorded under the cell-attached and inside–out configurations of the patch-clamp technique using an Axopatch 200A patch-clamp amplifier and pClamp8 data acquisition software (Molecular Devices). Electrodes were made from borosilicate glass (World Precision Instruments) using a Sutter P-97 microelectrode puller (Sutter Instrument) and had a tip diameter of 5–25 μm. Three sets of solutions were used on both sides of the membrane: (*i*) ND96K solution: (in mM) 96 KCl, 1 $MgCl_2$, 5 EGTA, and 10 Hepes (pH 7.4); (*ii*) FVPP solution: (in mM) 96 KCl, 5 EDTA, 10 Hepes, 5 NaF, 0.2 Na_3VO_4, and 10 Na_2PO_7 (pH 7.4) to delay PIP_2 dephosphorylation (19); and (*iii*) gating current solution: (in mM) 120 N-methyl-D-glucamine (NMG^+), 2 EGTA, 2 $Ca^{2+}MeSO^-_3$, and 10 Hepes (pH 7.4). Data were analyzed using the Clampfit 8 and Origin software.

Kv1.2 single-channel currents were recorded from oocytes under the standard inside–out patch configuration. The pipette solution contained (in mM) 96 K-MeS, 10 Hepes, and 2 mM $MgCl_2$, pH 7.4, adjusted with KOH. The composition of the bath solution was (in mM) 96 potassium 4-morpholineethanesulfonate (K-MeS), 10 Hepes, and 5 EGTA, pH 7.4, adjusted with KOH.

Single-channel conductance values were determined by the slope of current–voltage (i–V) curves where i–V data could be well fitted to a linear line. Open probability was determined simply by dividing the total open time by the sum of the open and closed times in patches containing only one channel. When multiple channels were present in the patch, open probability was determined from the amplitude histogram as P_o (%) = $(1 - P_C^{1/N}) \times 100$, where P_C is the fraction of area under the closed state, and N is the maximal number of simultaneous channel openings observed when the open probability was high (e.g., at positive voltages).

Chemicals. PIP_2 and diC8-PIP_2 and PIP_2 antibody were purchased from Avanti Polar Lipids, PIP_2-Ab was purchased from Enzo Life Sciences (formerly Assay Designs), and wortmannin was purchased from Sigma-Aldrich. PIP_2, diC8-PIP_2, and PIP_2-Ab were prepared as described previously (19, 28).

Data Analysis. Data in all figures are expressed as mean ± SEM. Statistical significance was evaluated by Student´s *t* test.

Homology Modeling for Kv1.2 Channel. ***Homology model construction.*** The crystal structure of the Kv1.2 channel [Protein Data Bank (PDB) ID 2A79; resolution: 2.9 Å] (23) is missing electron density in segments S1 and S3 and in the loops connecting segments S1, S2, S3, and S4. The most complete Kv channel crystal structure is the Kv1.2 and Kv2.1 chimera (PDB ID 2R9R; resolution: 2.4 Å) (9). The Kv1.2/2.1 channel chimera structure was used as a template to develop homology models for the Kv1.2 channel. We used the Kv1.2/2.1 chimera and the Kv1.2 channel (GenInfo Identifier: 52000923) for sequence alignment [ClustalW server (http://www.ebi.ac.uk/Tools/clustalw2/index.html)]. The Kv1.2/2.1 chimera was constructed mostly by the Kv1.2 channel. The sequence identity between the Kv1.2/2.1 chimera and the Kv1.2 channel is 93%. Only a small region (27 residues) between the S3 and S4 helices of the chimera structure came from the Kv2.1 channel. We replaced the Kv2.1 residues on the S3 and S4 helices of the Kv1.2/2.1 chimera structure with the corresponding Kv1.2 residues and regenerated an S3–S4 linker by using the loop structural template database search in the SYBYL graphic software package (Tripos Inc.). This regeneration was followed by energy minimizations using the SYBYL software package. The Kv1.2 model structure was evaluated by the PROCHECK program (33, 34) for the quality of the stereochemistry. The phi and psi distributions showed that in the final model 91% of residues were in the most favored regions of the Ramachandran plot, 9.0% of residues were in allowed regions, and none was in disallowed regions. This result compared favorably with the structure of the Kv1.2/2.1 crystal template, where 89.9% of residues were in the most favored regions, 11.1% of residues were in the allowed regions, and none was in the disallowed regions. The overall PROCHECK G-factor of the model was 0.0. All these assessments indicated that the model structure was reasonable.

PIP_2 and Kv1.2 Interactions. We used the AUTODOCK program (35) to dock the PIP_2 head group into the Kv1.2 model structure. AUTODOCK is an automatically flexible molecular docking program that can account for the flexibility of the PIP_2 head group during the docking simulations. The grid-based potential maps that were generated for the Kv1.2 channel using CHNOP (i.e., carbon, hydrogen, nitrogen, oxygen, and phosphorus) elements, sampled on a uniform grid containing 120 × 120 × 120 points, were 0.375 Å apart for the free-energy calculations. The grid box was centered at the geometrical center of residues K147, K322, and R326 of Kv1.2, which were found by our functional study to be important for PIP_2 sensitivity. The Lamarckian Genetic Algorithm was used to identify the binding conformations of the PIP_2 head group. One hundred docking simulations were performed. The final docked PIP_2 head group configurations were selected based on docked binding energies and cluster analysis. A potential binding site of the Kv1.2 channel for PIP_2 was identified by docking simulations, formed by positively charged residues K134, R138, K312, K322, and R419.
MD simulations. MD simulations (100 ns in duration) were conducted on Kv1.2 in the presence and absence of PIP_2. The channel was immersed in an explicit palmitoyl-oleoyl phosphatidylcholine bilayer of ~35-Å thicknesses. After being solvated with single point charge water molecules, neutralized by Na^+ as the counter ions, and including K^+ located in the selectivity filter obtained from the Kv1.2/2.1 crystal, each system used in the MD simulations had ~175,000 atoms. GROMACS v4.0.5 (36) was used to conduct the simulation with GROMOS96 53a6 force field (37).

ACKNOWLEDGMENTS. We thank the members of the D.E.L. laboratory, Qi Zhao Yuyang Zhang, and Shobana Sundaram for contributions to the initial phases of this project; Carlos Villalba-Galea for advice with gating current measurements; Heikki Vaananen and Sophia Gruszecki for oocyte isolation; members of the D.E.L. laboratory for critical input throughout the project; and Linda Boland, Louis J. De Felice, and Carlos Villalba-Galea for critical feedback on the manuscript. This work was supported by R01 Grant HL-59949 (to D.E.L.) and by discretionary funds by the Virginia Commonwealth University School of Medicine (to D.E.L.). Computations were supported by the Center for High Performance Computing at Virginia Commonwealth University and by National Institutes of Health Shared Instrumentation Grant S10RR027411 (to M.C.).

1. Bezanilla F, Perozo E, Stefani E (1994) Gating of Shaker K^+ channels: II. The components of gating currents and a model of channel activation. *Biophys J* 66: 1011–1021.
2. Zagotta WN, Hoshi T, Dittman J, Aldrich RW (1994) Shaker potassium channel gating. II: Transitions in the activation pathway. *J Gen Physiol* 103:279–319.
3. Smith-Maxwell CJ, Ledwell JL, Aldrich RW (1998) Role of the S4 in cooperativity of voltage-dependent potassium channel activation. *J Gen Physiol* 111:399–420.
4. Ledwell JL, Aldrich RW (1999) Mutations in the S4 region isolate the final voltage-dependent cooperative step in potassium channel activation. *J Gen Physiol* 113: 389–414.
5. Stühmer W, et al. (1989) Structural parts involved in activation and inactivation of the sodium channel. *Nature* 339:597–603.
6. Liman ER, Hess P, Weaver F, Koren G (1991) Voltage-sensing residues in the S4 region of a mammalian K^+ channel. *Nature* 353:752–756.
7. Logothetis DE, Movahedi S, Satler C, Lindpaintner K, Nadal-Ginard B (1992) Incremental reductions of positive charge within the S4 region of a voltage-gated K^+ channel result in corresponding decreases in gating charge. *Neuron* 8:531–540.
8. Long SB, Tao X, Campbell EB, MacKinnon R (2007) Atomic structure of a voltage-dependent K^+ channel in a lipid membrane-like environment. *Nature* 450:376–382.
9. Jiang Y, et al. (2003) X-ray structure of a voltage-dependent K^+ channel. *Nature* 423: 33–41.
10. Milescu M, et al. (2009) Interactions between lipids and voltage sensor paddles detected with tarantula toxins. *Nat Struct Mol Biol* 16:1080–1085.
11. Ramu Y, Xu Y, Lu Z (2006) Enzymatic activation of voltage-gated potassium channels. *Nature* 442:696–699.
12. Xu Y, Ramu Y, Lu Z (2008) Removal of phospho-head groups of membrane lipids immobilizes voltage sensors of K^+ channels. *Nature* 451:826–829.
13. Hilgemann DW, Feng S, Nasuhoglu C (2001) The complex and intriguing lives of PIP_2 with ion channels and transporters. *Sci STKE* 2001:re19.
14. Logothetis DE, Petrou VI, Adney SK, Mahajan R (2010) Channelopathies linked to plasma membrane phosphoinositides. *Pflugers Arch* 460:321–341.
15. Oliver D, et al. (2004) Functional conversion between A-type and delayed rectifier K^+ channels by membrane lipids. *Science* 304:265–270.
16. Murata Y, Iwasaki H, Sasaki M, Inaba K, Okamura Y (2005) Phosphoinositide phosphatase activity coupled to an intrinsic voltage sensor. *Nature* 435:1239–1243.
17. Kohout SC, et al. (2010) Electrochemical coupling in the voltage-dependent phosphatase Ci-VSP. *Nat Chem Biol* 6:369–375.
18. Hamill OP, Marty A, Neher E, Sakmann B, Sigworth FJ (1981) Improved patch-clamp techniques for high-resolution current recording from cells and cell-free membrane patches. *Pflugers Arch* 391:85–100.
19. Huang CL, Feng S, Hilgemann DW (1998) Direct activation of inward rectifier potassium channels by PIP_2 and its stabilization by Gbetagamma. *Nature* 391: 803–806.
20. Zhang H, He C, Yan X, Mirshahi T, Logothetis DE (1999) Activation of inwardly rectifying K^+ channels by distinct PtdIns(4,5)P_2 interactions. *Nat Cell Biol* 1:183–188.
21. Zhang H, et al. (2003) PIP(2) activates KCNQ channels, and its hydrolysis underlies receptor-mediated inhibition of M currents. *Neuron* 37:963–975.
22. Rosenhouse-Dantsker A, Logothetis DE (2007) Molecular characteristics of phosphoinositide binding. *Pflugers Arch* 455:45–53.
23. Long SB, Campbell EB, Mackinnon R (2005) Crystal structure of a mammalian voltage-dependent Shaker family K^+ channel. *Science* 309:897–903.
24. Pathak MM, et al. (2007) Closing in on the resting state of the Shaker K(+) channel. *Neuron* 56:124–140.
25. Khalili-Araghi F, et al. (2010) Calculation of the gating charge for the Kv1.2 voltage-activated potassium channel. *Biophys J* 98:2189–2198.
26. Hansen SB, Tao X, MacKinnon R (2011) Structural basis of PIP2 activation of the classical inward rectifier K^+ channel Kir2.2. *Nature* 477:495–498.
27. Suh BC, Hille B (2005) Regulation of ion channels by phosphatidylinositol 4,5-bisphosphate. *Curr Opin Neurobiol* 15:370–378.
28. Lopes CM, et al. (2002) Alterations in conserved Kir channel-PIP_2 interactions underlie channelopathies. *Neuron* 34:933–944.
29. Loussouarn G, et al. (2003) Phosphatidylinositol-4,5-bisphosphate, PIP2, controls KCNQ1/KCNE1 voltage-gated potassium channels: A functional homology between voltage-gated and inward rectifier K+ channels. *EMBO J* 22:5412–5421.
30. Villalba-Galea CA, Sandtner W, Starace DM, Bezanilla F (2008) S4-based voltage sensors have three major conformations. *Proc Natl Acad Sci USA* 105:17600–17607.
31. Börjesson SI, Hammarström S, Elinder F (2008) Lipoelectric modification of ion channel voltage gating by polyunsaturated fatty acids. *Biophys J* 95:2242–2253.
32. Wu L, Bauer CS, Zhen XG, Xie C, Yang J (2002) Dual regulation of voltage-gated calcium channels by PtdIns(4,5)P_2. *Nature* 419:947–952.
33. Kahraman A, Morris RJ, Laskowski RA, Thornton JM (2007) Shape variation in protein binding pockets and their ligands. *J Mol Biol* 368:283–301.
34. Morris AL, MacArthur MW, Hutchinson EG, Thornton JM (1992) Stereochemical quality of protein structure coordinates. *Proteins* 12:345–364.
35. Morris GM, et al. (1998) Automated docking using a lamarckian genetic algorithm and an empirical binding free energy function. *J Comput Chem* 19:1639–1662.
36. Hess B, Kutzner C, van der Spoel D, Lindahl E (2008) GROMACS 4: Algorithms for highly efficient, load-balanced, and scalable molecular simulation. *J Chem Theory Comput* 4:435–447.
37. Oostenbrink C, van Gunsteren WF (2004) Free energies of binding of polychlorinated biphenyls to the estrogen receptor from a single simulation. *Proteins* 54:237–246.